

Cite this: *J. Mater. Chem. C*,
2026, 14, 577Received 11th November 2025,
Accepted 19th December 2025

DOI: 10.1039/d5tc04007h

rsc.li/materials-c

Full-range luminescence color tuning from blue to red in generic single-boron multi-resonance delayed fluorescence emitters

Daiki Endo^a and Takuma Yasuda^{ib} *^{ab}

We report a family of sulfur-containing, single-boron multi-resonance thermally activated delayed fluorescence emitters that exhibit narrowband emissions spanning the full visible spectrum from blue to red. Site-specific incorporation of a carbazole unit and ring-fused π -extension with an indolocarbazole fragment enable extensive color tuning while maintaining sharp emission profiles.

Polycyclic aromatic hydrocarbons (PAHs) doped with heteroatoms have emerged as a prominent class of advanced organic functional materials owing to their tunable electronic structures and exceptional optoelectronic properties.^{1–4} Their frontier orbital distributions, energy gaps, and excited-state dynamics can be precisely modulated not only by controlling the size and topology of the π -conjugated framework but also through the deliberate incorporation of heteroatoms such as boron (B), nitrogen (N), oxygen (O), and sulfur (S). A major breakthrough in this field occurred in 2016, when Hatakeyama *et al.* developed B,N-doped PAHs, typified by DABNA, which exhibit narrowband thermally activated delayed fluorescence (TADF) arising from the multi-resonance (MR) effect.^{5,6} Since then, MR-TADF emitters have become key candidates for next-generation organic light-emitting diodes (OLEDs) that combine excellent color purity with high external quantum efficiency (EQE).^{7–11}

With the implementation of the BT.2020¹² wide-color-gamut standard for ultrahigh-definition displays, there has been a growing demand for organic emitters with precisely controlled electroluminescence (EL) spectra. Consequently, the development of narrowband MR-TADF emitters covering the entire visible range, particularly the red region, has become a central challenge in OLED research. Although numerous MR-TADF emitters exhibiting blue to green emissions have been

reported,^{5–11} efficient red organoboron MR emitters remain scarce^{13–30} (see SI for more details). The reported molecular design strategies for red MR-TADF can be broadly classified into three categories: (i) constructing *para*-D- π -D (D = N, O, S) and *para*-B- π -B architectures,^{13–15,17,18,21–23,29} (ii) introducing strong donor and acceptor substituents at the periphery,^{19,25,28} and (iii) expanding the π -conjugated MR core.^{16,20,26,27} However, these approaches often involve complex multistep synthetic routes and lead to high molecular weights, thereby limiting emitter design diversity.

Herein, we report a universal and synthetically simple design strategy that enables full-range emission color tuning—from blue to red—within a versatile single-boron MR-TADF framework. As the parent MR scaffold, we employed a S-containing MR core (CzBS),³¹ in which the S-induced heavy-atom effect facilitates the reverse intersystem crossing (RISC) process.^{31–33} CzBS exhibits sky-blue narrowband emission with a high photoluminescence (PL) quantum yield ($\Phi_{\text{PL}} = 99\%$) and high RISC rate ($k_{\text{RISC}} = 4 \times 10^5 \text{ s}^{-1}$). With this scaffold, CzBS-Cz1 (1) and CzBS-Cz2 (2) were developed by introducing an additional carbazole fragment in the *para*-B- π -N and *para*-N- π -S fashions, respectively (Fig. 1a), leading to hypsochromic and bathochromic spectral shifts.³⁴ Furthermore, IDCzBS (3) was designed *via* a novel ring-fused π -extension, which induced a further bathochromic shift into the red region. Remarkably, 3 (M.W. = 446) represents the most compact red MR-TADF emitter reported to date (SI), demonstrating that even a minimal single-boron MR core can deliver efficient narrowband red TADF. This conceptually simple yet powerful strategy thus provides a broadly applicable platform for color-tunable MR-TADF emitters compatible with wide-color-gamut OLEDs.

Compounds 1–3 were synthesized in three steps starting from commercially available haloarene (SI). The synthetic sequence comprises: (i) nucleophilic aromatic substitution ($\text{S}_{\text{N}}\text{Ar}$) to introduce carbazole or indolocarbazole moieties, (ii) sulfidation using benzenethiol *via* $\text{S}_{\text{N}}\text{Ar}$ or Pd-catalyzed C–S cross-coupling,³⁵ and (iii) intramolecular borylation *via* one-pot tandem lithiation–borylation–annulation.^{5,13} Notably, the $\text{S}_{\text{N}}\text{Ar}$ reaction with

^a Department of Applied Chemistry, Graduate School of Engineering, Kyushu University, 744 Motoooka, Nishi-ku, Fukuoka 819-0395, Japan.
E-mail: yasuda@ifrc.kyushu-u.ac.jp

^b Institute for Advanced Study, Kyushu University, 744 Motoooka, Nishi-ku, Fukuoka 819-0395, Japan



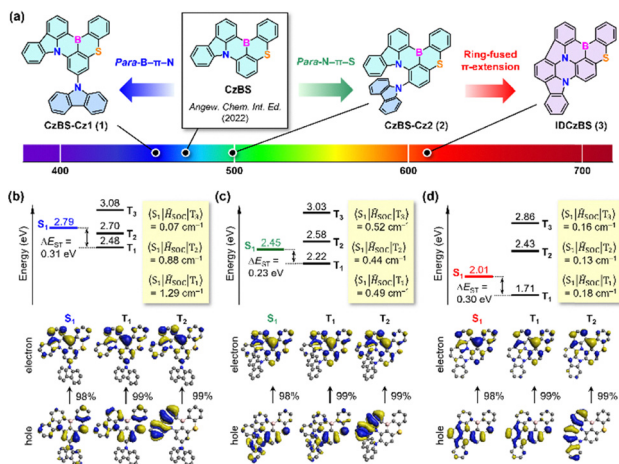


Fig. 1 (a) Molecular design strategy for achieving blue-to-red narrow-band emissions based on the single-boron MR framework of **CzBS**. (b)–(d) Simulated energy-level diagrams and natural transition orbital (NTO) representations of the excited singlet (S_1) and triplet (T_1 – T_3) states for (b) **1**, (c) **2**, and (d) **3**, calculated using TDDFT at the PBE0/DZP level.

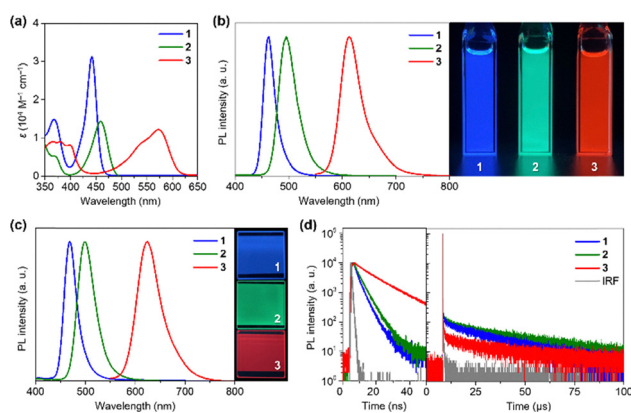


Fig. 2 (a) UV-vis absorption and (b) PL spectra with corresponding emission photographs of **1–3** in toluene (10^{-5} M). (c) Steady-state PL spectra and emission photographs, and (d) transient PL decay curves of the doped films of **1–3** in mCBP host matrices at a doping concentration of 1 wt%. IRF denotes the instrument response function.

dihydroindolo[2,3-*a*]carbazole in the synthesis of **3** proceeded smoothly, affording a highly π -extended PAH framework incorporating two adjacent N atoms. Thermogravimetric analysis revealed high thermal decomposition temperatures (T_d , 5% weight loss) of 419, 394, and 449 °C for **1–3**, respectively, confirming their excellent thermal stability and suitability for vacuum thermal evaporation in OLED fabrication.

Time-dependent density functional theory (TDDFT) calculations predicted the lowest-excited singlet (S_1) energies of **1–3** to be 2.79, 2.45, and 2.01 eV, respectively (Fig. 1b–d), indicating that their emission color can be tuned from blue to red. The corresponding spin–orbit coupling (SOC) matrix element ($\langle S_1 | \hat{H}_{\text{SOC}} | T_1 \rangle$), which plays a pivotal role in governing the spin–flip RISC process, was calculated to be 1.29, 0.49, and 0.18 cm^{-1} for **1–3**, respectively. The relatively large SOC values for **1** and **2** can be attributed to the S-induced heavy-atom effect, suggesting efficient RISC processes comparable to those of the parent **CzBS**.³¹ In contrast, the π -extension in **3** attenuated the S-induced electronic perturbation, resulting in a reduced SOC value.

Subsequently, the photophysical properties of **1–3** were examined in dilute toluene solutions and in doped films employing 3,3'-di(carbazol-9-yl)-1,1'-biphenyl (mCBP) as the host matrix (Fig. 2 and Table 1). As expected, the absorption and emission maxima ($\lambda_{\text{abs}}/\lambda_{\text{PL}}$) in solution exhibited systematic bathochromic shifts in the order of **1** (442/463 nm), **2** (459/495 nm), and **3** (573/612 nm), corresponding to blue, green, and red emissions, respectively (Fig. 2a and b). The Φ_{PL} values in toluene were 95%, 90%, and 73% for **1–3**, respectively. The lower Φ_{PL} observed for **3** was attributed to enhanced nonradiative decay pathways associated with the energy-gap law.^{36,37} In the doped films, the PL spectra of **1–3** (Fig. 2d) showed modest bathochromic shifts (by 4–13 nm) and slightly broader full width at half maxima (FWHMs) relative to their solution states, likely because of host–guest electronic interactions. The Φ_{PL} values of **1** and **2** remained high (>90%), whereas that of **3** was somewhat decreased, presumably because of incomplete excited energy transfer from the host to the emitter. The singlet–triplet energy gaps (ΔE_{ST}) of **1–3**, estimated from their fluorescence and phosphorescence spectra, were comparably small (0.12–0.15 eV, Table 1 and SI), confirming the feasibility of the RISC process.

Table 1 Photophysical data of MR-TADF emitters **1–3**

Emitter	State ^a	λ_{PL}^b (nm)	FWHM ^c (nm eV ⁻¹)	Φ_{PL}^d (%)	Φ_{p}^e (%)	Φ_{d}^e (%)	τ_{p}^f (ns)	τ_{d}^f (μs)	k_{r}^g (10^7 s^{-1})	k_{ISC}^h (10^7 s^{-1})	k_{RISC}^i (10^5 s^{-1})	ΔE_{ST}^j (eV)
1	Sol	463	25/0.15	95	23	72	2.9	37	8.0	27	1.1	0.13
	Film	468	30/0.17	91	23	68	3.4	25	6.7	23	1.6	0.14
2	Sol	495	39/0.20	90	24	66	3.0	25	8.1	25	1.4	0.13
	Film	499	41/0.21	91	20	71	4.0	31	5.1	20	1.4	0.15
3	Sol	612	46/0.15	73	73	~0	9.8	—	7.5	—	—	0.12
	Film	625	55/0.17	53	34	19	13	46	2.6	5.0	0.18	0.12

^a Sol = deoxygenated toluene solution (10^{-5} M); film = 1 wt%-doped film in an mCBP host matrix. ^b PL emission maximum. ^c Full width at half-maximum of the PL spectrum given in wavelength and energy. ^d Absolute PL quantum yield evaluated using an integrating sphere. ^e Fractional quantum yields for prompt fluorescence (Φ_{p}) and delayed fluorescence (Φ_{d}); $\Phi_{\text{p}} + \Phi_{\text{d}} = \Phi_{\text{PL}}$. ^f Emission lifetimes for prompt fluorescence (τ_{p}) and delayed fluorescence (τ_{d}). ^g Rate constant of fluorescence radiative decay ($S_1 \rightarrow S_0$); $k_{\text{r}} = \Phi_{\text{p}}/\tau_{\text{p}}$. ^h Rate constant of ISC ($S_1 \rightarrow T_1$); $k_{\text{ISC}} = (1 - \Phi_{\text{p}})/\tau_{\text{p}}$. ⁱ Rate constant of RISC ($T_1 \rightarrow S_1$); $k_{\text{RISC}} = \Phi_{\text{d}}/(k_{\text{ISC}} \tau_{\text{p}} \tau_{\text{d}} \Phi_{\text{p}})$. ^j Singlet–triplet energy gap estimated from the λ_{PL} positions of fluorescence and phosphorescence spectra.



Transient PL decay profiles of **1–3** in the doped films revealed distinct TADF behavior, featuring nanosecond-scale prompt and microsecond-scale delayed emission components (Fig. 2d). From these data, the photophysical rate constants for radiative decay (k_r), intersystem crossing (k_{ISC}), and RISC (k_{RISC}) were determined (Table 1). Owing to the MR effect, all emitters exhibited large k_r values exceeding 10^7 s^{-1} . Compounds **1** and **2** showed relatively high k_{RISC} values on the order of 10^5 s^{-1} , consistent with the enhanced SOC induced by the heavy-atom effect. In contrast, **3** exhibited a k_{RISC} value approximately one order of magnitude lower than those of **1** and **2**, reflecting its reduced SOC (Fig. 1b).

To evaluate the EL performance of **1–3** as MR-TADF emitters, OLEDs were fabricated with the configuration: indium tin oxide (ITO, 50 nm)/2,3,6,7,10,11-hexacyano-1,4,5,8,9,12-hexaazatriphenylene (HAT-CN, 10 nm)/1,1-bis[(di-4-tolylamino)phenyl]-cyclohexane (TAPC, 40 nm)/1,3-bis(1,8-dimethylcarbazol-9-yl)-benzene (mMCP, 5 nm)/1 wt%-emitter: mCBP (30 nm)/2,8-bis(diphenylphosphinyl)dibenzo[*b,d*]furan (PPF, 5 nm)/1,3-bis-[3,5-di(pyridin-3-yl)phenyl]benzene (B3PyPB, 40 nm)/8-quinololato lithium (Liq, 1 nm)/Al (100 nm).³¹ The molecular structures of these materials and corresponding energy-level diagram of the devices are shown in the SI.

The OLEDs incorporating **1–3** exhibited sharp EL emissions with narrow FWHMs of 0.16–0.21 eV, corresponding to blue ($\lambda_{\text{EL}} = 464 \text{ nm}$), green (493 nm), and red (617 nm) emissions, respectively (Fig. 3a). The Commission Internationale de l'Éclairage (CIE) chromaticity coordinates were (0.13, 0.08) for **1**, (0.11, 0.43) for **2**, and (0.64, 0.35) for **3**, demonstrating full-color tunability even at the device level (Fig. 3b). The OLEDs achieved maximum EQE (EQE_{max}) of 21.4%, 20.7%, and 11.9% for **1–3**, respectively (Fig. 3c and d, and Table 2), consistent with their Φ_{PL} values and TADF properties in the doped films. At a luminance of 1000 cd m^{-2} , the corresponding EQE_{1000} values

Table 2 OLED performance data

Emitter	1	2	3
λ_{EL}^a (nm)	464	493	617
FWHM ^b (nm eV ⁻¹)	28/0.16	42/0.21	64/0.21
V_{on}^c (V)	4.8	4.6	5.6
$\text{EQE}_{\text{max}}^d$ (%)	21.4	20.7	11.9
$\text{EQE}_{100/1000}^e$ (%)	19.3/12.0	18.5/12.7	7.2/2.1
CIE (x, y) ^f	(0.13, 0.08)	(0.11, 0.43)	(0.64, 0.35)
CE^g (cd A ⁻¹)	15.8	44.5	15.6
PE^h (lm W ⁻¹)	10.0	27.7	8.5

^a EL emission maximum at 1 mA cm^{-2} . ^b Full width at half-maximum of the EL spectrum given wavelength and energy. ^c Turn-on voltage at a luminance above 1 cd m^{-2} . ^d Maximum external EL quantum efficiency. ^e External EL quantum efficiencies at luminances of 100 and 1000 cd m^{-2} . ^f CIE chromaticity coordinates. ^g Maximum current efficiency. ^h Maximum power efficiency.

were 12.0%, 12.7%, and 2.1%, representing roll-off ratios of approximately 44%, 39%, and 82%, respectively. The smaller efficiency roll-offs observed for **1** and **2** are attributed to their relatively high k_{RISC} values, comparable to that of **CzBS**. In contrast, the pronounced roll-off in the **3**-based device likely originates from its lower k_{RISC} . In this case, a large accumulation of triplet excitons occurs at high excitation densities, leading to detrimental exciton losses *via* triplet-triplet annihilation (TTA) and singlet-triplet annihilation (STA).³⁸ This issue can potentially be mitigated by optimizing the emission layer through the introduction of a suitable TADF or phosphorescent sensitizer.³⁹

Conclusions

In summary, we developed a series of S-containing, single-boron MR-TADF emitters that exhibited narrowband emissions spanning the entire visible range from blue to red. Notably, the ring-fused π -extension approach proved highly effective in inducing pronounced bathochromic shifts toward the red region, even within a structurally simple single-boron MR framework. This molecular design strategy provides valuable guidance for accessing low-energy narrowband emitters—an area long considered challenging—and expands the structural design landscape for red and near-infrared MR-TADF materials. We anticipate that further molecular refinements and device engineering will enable high-performance red narrowband OLEDs that combine exceptional color purity with high EL efficiency.

Author contributions

Daiki Endo: conceptualization, investigation, writing – original draft, review & editing. Takuma Yasuda: conceptualization, project management, supervision, resources, writing – original draft, review & editing.

Conflicts of interest

There are no conflicts to declare.

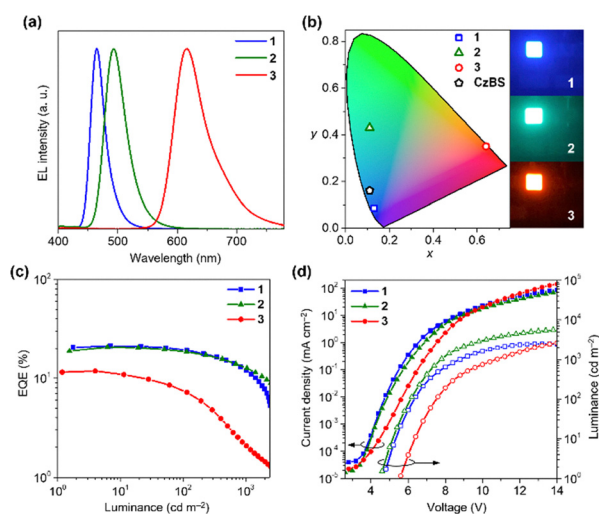


Fig. 3 OLED characteristics of the **CzBS**-derived MR-TADF emitters **1–3**. (a) EL spectra recorded at 1 mA cm^{-2} , (b) EL emission images and corresponding CIE chromaticity coordinates. (c) External quantum efficiency–luminance (EQE-L) plots, and (d) current density–voltage–luminance ($J-V-L$) characteristics.



Data availability

The data supporting this article have been included within the manuscript and its supplementary information (SI). Supplementary information: synthetic procedures, characterization data, supplementary figures, and detailed information. See DOI: <https://doi.org/10.1039/d5tc04007h>.

Acknowledgements

This work was supported in part by JSPS KAKENHI (Grant No. JP24K21248 and JP25K01848), JST CREST (Grant No. JPMJCR21O5), the Hosono Bunka Foundation, the Iketani Science and Technology Foundation, and the Kuma Foundation. The authors gratefully acknowledge Ms Nanami Kubo and Ms Hiroko Nomura for their technical assistance. The authors also thank the Cooperative Research Program of Network Joint Research Center for Materials and Devices (NJRC), the Advanced Research Infrastructure for Materials and Nanotechnology in Japan (ARIM) of MEXT, and the Research Institute for Information Technology at Kyushu University for their generous research support.

References

- M. Stępień, E. Gońka, M. Żyła and N. Sprutta, *Chem. Rev.*, 2017, **117**, 3479–3716.
- A. Borissov, Y. K. Maurya, L. Moshniha, W.-S. Wong, M. Żyła-Karwowska and M. Stępień, *Chem. Rev.*, 2022, **122**, 565–788.
- M. Hirai, N. Tanaka, M. Sakai and S. Yamaguchi, *Chem. Rev.*, 2019, **119**, 8291–8331.
- X.-Y. Wang, X. Yao, A. Narita and K. Müllen, *Acc. Chem. Res.*, 2019, **52**, 2491–2505.
- T. Hatakeyama, K. Shiren, K. Nakajima, S. Nomura, S. Nakatsuka, K. Kinoshita, J. Ni, Y. Ono and T. Ikuta, *Adv. Mater.*, 2016, **28**, 2777–2781.
- Y. Kondo, K. Yoshiura, S. Kitera, H. Nishi, S. Oda, H. Gotoh, Y. Sasada, M. Yanai and T. Hatakeyama, *Nat. Photonics*, 2019, **13**, 678–682.
- H. J. Kim and T. Yasuda, *Adv. Opt. Mater.*, 2022, **10**, 2201714.
- H. Jiang, J. Jin and W.-Y. Wong, *Adv. Funct. Mater.*, 2023, **33**, 2306880.
- M. Mamada, M. Hayakawa, J. Ochi and T. Hatakeyama, *Chem. Soc. Rev.*, 2024, **53**, 1624–1692.
- J. Kang, D. J. Shin and J. Y. Lee, *Adv. Opt. Mater.*, 2025, **13**, 2402653.
- Y. Li, X. Tan, B. Cai and C.-Y. Chan, *Adv. Opt. Mater.*, 2025, **13**, 2403556.
- International Telecommunication Union (ITU-R), “Recommendation ITU-R BT. 2020: Parameter values for ultra-high definition television systems for production and international programme exchange”.
- M. Yang, I. S. Park and T. Yasuda, *J. Am. Chem. Soc.*, 2020, **142**, 19468–19472.
- Y. Zhang, D. Zhang, T. Huang, A. J. Gillett, Y. Liu, D. Hu, L. Cui, Z. Bin, G. Li, J. Wei and L. Duan, *Angew. Chem., Int. Ed.*, 2021, **60**, 20498–20503.
- J.-K. Li, X.-Y. Chen, Y.-L. Guo, X.-C. Wang, A. C.-H. Sue, X.-Y. Cao and X.-Y. Wang, *J. Am. Chem. Soc.*, 2021, **143**, 17958–17963.
- K. R. Naveen, S. J. Hwang, H. Lee and J. H. Kwon, *Adv. Electron. Mater.*, 2022, **8**, 2101114.
- Y. Zou, J. Hu, M. Yu, J. Miao, Z. Xie, Y. Qiu, X. Cao and C. Yang, *Adv. Mater.*, 2022, **34**, 2201442.
- Y. Wang, K. Zhang, F. Chen, X. Wang, Q. Yang, S. Wang, S. Shao and L. Wang, *Chin. J. Chem.*, 2022, **40**, 2671–2677.
- X. Cai, Y. Xu, Y. Pan, L. Li, Y. Pu, X. Zhuang, C. Li and Y. Wang, *Angew. Chem., Int. Ed.*, 2023, **62**, e202216473.
- H. Chen, T. Fan, G. Zhao, D. Zhang, G. Li, W. Jiang, L. Duan and Y. Zhang, *Angew. Chem., Int. Ed.*, 2023, **62**, e20230093.
- J.-K. Li, M.-Y. Zhang, L. Zeng, L. Huang and X.-Y. Wang, *Angew. Chem., Int. Ed.*, 2023, **62**, e202303093.
- T. Fan, M. Du, X. Jia, L. Wang, Z. Yin, Y. Shu, Y. Zhang, J. Wei, D. Zhang and L. Duan, *Adv. Mater.*, 2023, **35**, 2301018.
- T. Hua, N. Li, Z. Huang, Y. Zhang, L. Wang, Z. Chen, J. Miao, X. Cao, X. Wang and C. Yang, *Angew. Chem., Int. Ed.*, 2024, **63**, e202318433.
- M. Hayakawa, X. Tang, Y. Ueda, H. Eguchi, M. Kondo, S. Oda, X.-C. Fan, G. N. I. Lestanto, C. Adachi and T. Hatakeyama, *J. Am. Chem. Soc.*, 2024, **146**, 18331–18340.
- H. Wang, Y.-C. Cheng, X.-C. Fan, D.-Y. Chen, X. Xiong, X.-Y. Hao, Y.-Z. Shi, J. Yu, D. Huang, J.-X. Chen, K. Wang and X.-H. Zhang, *Sci. Bull.*, 2024, **69**, 2983–2986.
- Y.-Y. Ju, L.-E. Xie, J.-F. Xing, Q.-S. Deng, X.-W. Chen, L.-X. Huang, G.-H. Nie, Y.-Z. Tan and B. Zhang, *Angew. Chem., Int. Ed.*, 2025, **64**, e202414383.
- H. Chen, M. Du, C. Qu, Q. Jin, Z. Tao, R. Ji, G. Zhao, T. Zhou, Y. Lou, Y. Sun, W. Jiang, L. Duan and Y. Zhang, *Angew. Chem., Int. Ed.*, 2025, **64**, e202415400.
- L. Ge, W. Zhang, Y.-H. Hao, M. Li, Y. Liu, M. Zhou and L.-S. Cui, *J. Am. Chem. Soc.*, 2024, **146**, 32826–32836.
- Y. Pu, Q. Jin, Y. Zhang, L. Duan and Y. Wang, *Nat. Commun.*, 2025, **16**, 332.
- J. Zhang, J. Liu, Y. He, G. Gao, X.-K. Chen, C. Yang and Z. Bin, *Angew. Chem., Int. Ed.*, 2025, **64**, e202520322.
- I. S. Park, H. Min and T. Yasuda, *Angew. Chem., Int. Ed.*, 2022, **61**, 202205684.
- M. Nagata, H. Min, E. Watanabe, H. Fukumoto, Y. Mizuhata, N. Tokitoh, T. Agou and T. Yasuda, *Angew. Chem., Int. Ed.*, 2021, **60**, 20280–20285.
- I. S. Park, M. Yang, H. Shibata, N. Amanokura and T. Yasuda, *Adv. Mater.*, 2022, **34**, 2107951.
- Y. Xu, C. Li, Z. Li, Q. Wang, X. Cai, J. Wei and Y. Wang, *Angew. Chem., Int. Ed.*, 2020, **59**, 17442–17446.
- T. Itoh and T. Mase, *Org. Lett.*, 2004, **6**, 4587–4590.
- J. V. Caspar, E. M. Kober, B. P. Sullivan and T. J. Meyer, *J. Am. Chem. Soc.*, 1982, **104**, 630–632.
- J. V. Caspar and T. J. Meyer, *J. Phys. Chem.*, 1983, **87**, 952–957.
- C. Murawski, K. Leo and M. C. Gather, *Adv. Mater.*, 2013, **25**, 6801–6827.
- H. Nakanotani, T. Higuchi, T. Furukawa, K. Masui, K. Morimoto, M. Numata, H. Tanaka, Y. Sagara, T. Yasuda and C. Adachi, *Nat. Commun.*, 2014, **5**, 4016.

